aerospace

MDPI

Article

Design and Analysis of a Micro–Electro-Mechanical System Thruster for Small Satellites and Low-Thrust Propulsion

Yubin Zhong [1,2,*], Fabrizio Ponti [3], Francesco Barato [4], Guojun Xia [1,2], Siyu Li [1,2], Xiao Zhang [1,2] and Tao Wu [1,2]

[1] Deep Space Exploration Laboratory, Hefei 230000, China; xiaguojun90@163.com (G.X.); lisiyv@mail.ustc.edu.cn (S.L.); zxhit509@126.com (X.Z.); wutaoxs@ustc.edu (T.W.)
[2] National Key Laboratory of Deep Space Exploration, Hefei 230000, China
[3] Department of Industrial Engineering (DIN), University of Bologna, 47122 Forlì, Italy; fabrizio.ponti@unibo.it
[4] Department of Industrial Engineering (DII), University of Padova, 35131 Padua, Italy; francesco.barato@unipd.it
* Correspondence: yubin.zhong@studio.unibo.it

Abstract: As a cost-effective and versatile solution, small satellites are increasingly being considered for space exploration. However, one of the major challenges in deploying small satellites for high total impulse missions, particularly deep space exploration, lies in the propulsion system. These missions face strict constraints in terms of volume, mass, and power budgets. This paper proposes a potential solution to this issue through the design of a bipropellant MEMS thruster. Simulation results indicate that this type of thruster offers superior performance compared to the monopropellant propulsion systems typically used in small satellite missions. Specifically, the bipropellant MEMS thruster demonstrates enhanced specific impulse and thrust-to-weight ratio, making it a promising alternative for small satellite propulsion in high total impulse missions.

Keywords: MEMS propulsion; small satellites; green propellant; low-thrust propulsion; spacecraft design

Academic Editor: Jae Hyun Park

Received: 31 December 2024
Revised: 17 February 2025
Accepted: 20 February 2025
Published: 21 February 2025

Citation: Zhong, Y.; Ponti, F.; Barato, F.; Xia, G.; Li, S.; Zhang, X.; Wu, T. Design and Analysis of a Micro–Electro-Mechanical System Thruster for Small Satellites and Low-Thrust Propulsion. *Aerospace* **2025**, *12*, 172. https://doi.org/10.3390/aerospace12030172

1. Introduction

Micro–Electro-Mechanical System (MEMS) thrusters are gaining increasing attention due to the growing demand for small satellites in space exploration [1–4]. Small satellites, particularly CubeSats and other small form-factor spacecraft, are designed with strict limitations on mass, volume, and financial budgets. These constraints pose significant challenges for propulsion system integration, as traditional and electric propulsion technologies tend to be bulky, power-hungry, and costly [5,6]. MEMS thrusters, manufactured using MEMS technology—a process similar to integrated circuit production—offer several key advantages, including mass production capabilities, compact size, and low mass, making MEMS thrusters highly suitable for small satellite missions [7,8].

The application of MEMS fabrication techniques provides several distinct benefits. MEMS thrusters have a high thrust-to-weight ratio due to their lightweight design, and they are cost-effective to produce, thanks to their suitability for mass production [9,10]. Bipropellant MEMS thrusters particularly benefit from MEMS technology because they offer high thrust per unit area while enabling complex structural designs. For the same thrust, the thrust chamber of a bipropellant MEMS thruster is much smaller than that of monopropellant or electric thrusters. This advantage becomes even more significant for low-thrust applications (below 1 N), which are common for CubeSats. Since CubeSats

generally have standardized frames, the volume of subsystems is a critical factor. A smaller thruster saves valuable space, allowing for more propellant or payload, thus extending the satellite's operational lifetime with more fuel or enabling additional functionality with extra payload.

In addition, MEMS-based bipropellant thrusters offer a power advantage compared to electric thrusters. While electric propulsion systems, such as Hall thrusters, offer much higher specific impulse, they require substantial power. For example, a 0.08 N Hall thruster developed by SERAN Systems demands 1350 W of power, which places considerable constraints on small satellite power budgets [11]. In contrast, a bipropellant MEMS requires peak power only during ignition, allowing the satellite to allocate a larger portion of its power budget to the mission itself.

Since the 1990s, MIT has been developing bipropellant MEMS thrusters powered by hydrogen and oxygen [12]. At the time, the thrust-to-weight ratio of these thrusters reached 85:1 and could exceed 1000:1 with a power density of 400 W/m^2 under full design conditions—figures that are almost impossible to achieve with traditional large-scale rockets. For comparison, this performance is nearly 100 times greater than that of the LEROS 1b thruster, which powers NASA's Juno deep space probe. However, hydrogen and oxygen require cryogenic storage and pose additional challenges, such as the corrosive nature of liquid hydrogen [13,14]. These factors necessitate a complex and heavy propellant tank, which contradicts the size and weight constraints of small satellites. To better suit small satellite missions, new propellant combinations must be explored. Ethane (C_2H_6) and nitrous oxide (N_2O), recognized as "green propellants", offer promising alternatives due to their favorable performance and easier storage conditions [15]. Thus, a bipropellant MEMS thruster using ethane–nitrous oxide (C_2H_6-N_2O) is proposed, and its performance is analyzed through simulation methods.

Preliminary simulation results suggest that reducing the engine size while maintaining constant chamber pressure leads to an increased thrust-to-weight ratio. Thrust is proportional to the throat area, while the engine weight scales with its volume. For ideal scaling, the ratio of the throat area to the overall volume increases as the engine size decreases. However, if traditional manufacturing methods are used, the cost of producing a smaller engine may not decrease proportionally compared to a full-size engine, and performance may not scale optimally. Previous research indicates that the thrust-to-weight ratio decreases as the engine volume decreases. This is where MEMS fabrication plays a critical role—as propulsion systems and spacecraft continue to shrink, the mass and volume savings from MEMS become increasingly significant. The performance of MEMS thrusters, particularly in terms of thrust-to-weight ratio, has already approached or even surpassed that of large-scale engines used for launch vehicles, making thrust-to-weight ratios above 1000 theoretically achievable for small thrusters.

2. Baseline Design

2.1. Concept and Propellant Selection

Silicon carbide (SiC) is selected as the fabrication material for the thruster due to its advanced thermo-mechanical properties, positioning it as a next-generation MEMS material. Compared to silicon, which is the most commonly used material in MEMS devices today, SiC offers superior performance in high-temperature and high-stress environments. With a melting point around 3000 K and a failure stress of approximately 400 MPa at 300 K [16,17], SiC can withstand the extreme temperatures and pressures encountered during combustion. As a result, the thruster can be fabricated using less material and without the need for an extensive cooling system, while still maintaining the robustness required for demanding operational conditions. The properties of Silicon and Silicon Carbide can be found in Table 1.

Table 1. Properties of material candidates for MEMS systems [12,18,19].

Properties	Si	SiC
Thermal Expansion Coefficient, $\times 10^{-6}$	2.6	4
Young's Modulus, GPa	170	400
Thermal Conductivity, W/(m·K)	148	100
Failure Stress at ~300 K, MPa	300	400
Melting Point, °C	1410	2730

To meet the stringent volume and mass constraints of small satellites, the propulsion system must be as simple and compact as possible. This is primarily achieved by employing simplified propellant feed systems, such as self-pressurized or gas-pressurized feed systems. For the propellants, both the fuel and oxidizer must be sufficiently stable to avoid overly complex propellant tanks designed to maintain cryogenic conditions, containment, or other specific requirements. Additionally, the propellant mixture should be easy to vaporize and ignite, which reduces the performance demands on the pre-heater and ignition systems [12,20].

For all these reasons, ethane (C_2H_6) and nitrous oxide (N_2O) are selected as the fuel and oxidizer for the propulsion system. These two propellants are considered green propellants due to their environmentally friendly combustion products, low toxicity, and favorable storage characteristics. When stored separately, ethane and nitrous oxide exhibit stable physical and chemical properties, minimizing the risks of deterioration, corrosion, or spontaneous combustion during long-term storage. At a storage temperature of 25 °C, ethane has a saturation pressure of approximately 42 bar, while nitrous oxide has a saturation pressure of about 56 bar. These similar storage conditions allow for the use of a common bulkhead (CBH) tank. Since the thruster operates as a self-pressurized system, the pressure and thrust performance will gradually decrease as the working fluid is consumed. The initial operating pressure is set at 15 bar, with an oxidizer-to-fuel (O/F) ratio of 4, corresponding to a fuel-rich design. This choice is made to reduce the combustion temperature, extend the thruster's lifetime, and minimize the need for an additional cooling system.

The performance of the system was initially predicted using the CEARUN program, with combustion pressure and expansion ratio as input parameters. While the program considers chemical equilibrium, the results reflect an idealized combustion scenario based on the chosen parameters. All coefficients are listed in Table 2.

Table 2. Propellant profile and predicted performance (at 15 bar and O/F = 4).

Composition	Fractions in CEARUN	Corrected Fractions in the Equation
Ethane, C_2H_6	/	145
Nitrous Oxide, N_2O	/	396
Methane, CH_4	0.00360	4
Carbon Oxide, CO	0.19412	216
Carbon Dioxide, CO_2	0.06278	70
Hydrogen Atom, H	0.00000	0
Hydrogen Cyanide, HCN	0.00000	0
Hydrogen, H_2	0.34728	387
Water, H_2O	0.03626	40
Ammonia, NH_3	0.00001	0
Nitric Oxide, NO	0.00000	0
Nitrogen, N_2	0.35594	396
Oxygen Atom, O	0.00000	0
Hydroxide Radical, OH	0.00000	0

Based on these results, the combustion reaction can be simplified as follows:

$$145C_2H_6 + 396N_2O = 4CH_4 + 216CO + 70CO_2 + 387H_2 + 40H_2O + 396N_2, \quad (1)$$

Table 3 shows that the precision of this equation simplification is sufficiently acceptable.

Table 3. Comparison of Products Fractions between CEARUN and Deducted Equation.

Composition	Fractions in CEARUN	Corrected Fractions in the Equation
CH_4	0.00360	0.00359
CO	0.19412	0.19407
CO_2	0.06278	0.06289
H_2	0.34728	0.34771
H_2O	0.03626	0.03594
N_2	0.35594	0.35580

The coefficients and fractions would be the reference for analyzing the CFD simulation. The detailed analysis is explained in Section 3.1.

2.2. Influence of MEMS Structure

Figure 1 illustrates a typical production process of a MEMS. A MEMS consists of multiple layers, with circuits and other structures integrated into each layer. These layers are typically fabricated using etching techniques, which result in a fixed notch width. As a result, it is not feasible to fabricate a complete Laval nozzle or a cylindrical channel extending from the inlet to the outlet on a single layer. Consequently, the segmented surfaces of the system are usually aligned parallel to the fluid flow. Due to this unique manufacturing process, the chamber and nozzle of a MEMS propulsion system are more likely to take the form of a rectangular channel rather than the cylindrical channel typically found in conventional rocket engines. While the top view of the thruster retains the shape of a Laval nozzle, the cross-sectional geometry at any given point is rectangular. The entire thruster is divided into layers, with each layer incorporating different components of the system, such as the propellant channels, combustion chamber, nozzle, and propellant injectors.

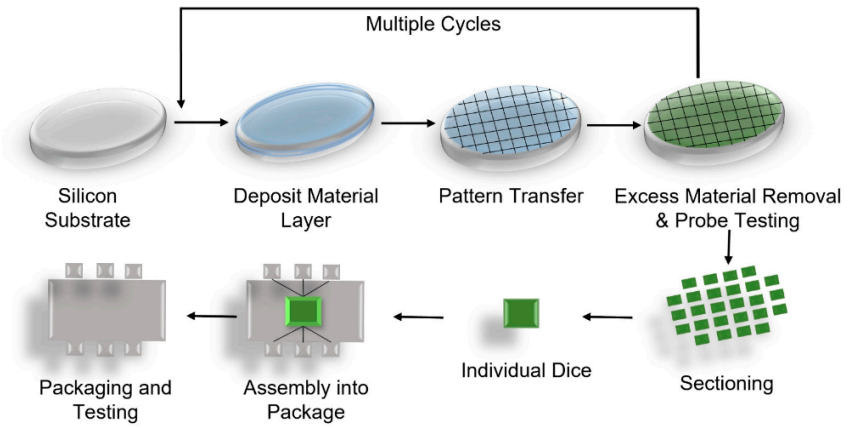

Figure 1. MEMS manufacturing process [21].

The injectors are positioned on the lateral walls of the combustion chamber, arranged in alternating parallel lines of the fuel and the oxidizer. These injectors are designed so that those on opposite walls inject different propellants in a way that each fuel jet aligns with and impinges on an oxidizer jet from the opposite wall, and vice versa. From a manufacturing perspective, this design is compatible with MEMS fabrication constraints.

From a performance standpoint, this configuration aims to ensure effective propellant mixing, as the opposing injection flows directly collide. However, due to the limited number of similar designs and studies, further simulations and experimental validation are required to confirm the actual effects of this configuration.

Another consequence of this unique geometry is its impact on the expansion ratio. Theoretically, the performance of the thruster improves with an increasing expansion ratio. In a conventional rocket with a circular throat and exit, the expansion ratio increases quadratically with the exit width, assuming a constant throat area. In contrast, for MEMSs, the relationship is linear, which limits the maximum expansion ratio achievable by the nozzle design. However, recent research from DLR indicates that an excessively large expansion ratio can paradoxically hinder fluid movement in a micro-scale planar nozzle due to the dominance of boundary layers in laminar flow [22]. This finding reduces the impact of the expansion ratio limitation on the overall thruster performance.

2.3. Preliminary Design

The combustion chamber of the baseline design is longer than that of a conventional system to ensure complete combustion before the flow reaches the throat. Since there is no precise method to predict the effect of cross-flow on reaction efficiency, the optimal design of the combustion chamber must be analyzed based on the simulation results of the reaction within this extended length.

As previously mentioned, the geometry is etched into silicon carbide, resulting in a high aspect ratio and a rectangular cross-section. The distance from the throat to the exit is 4.6 mm, with a throat width of 0.3 mm and a nozzle depth of 1 mm. The combustion chamber is 9.6 mm long and 4.0 mm wide. The exit width is 1.5 times that of the combustion chamber, yielding an exit width of 6 mm. In this design, the expansion ratio is set to 20, with the exit width being the upper limit of the design. This constraint aims to control the overall size of the thruster. Subsequent simulations will investigate the effects of wider exit widths on performance.

The propellant injectors are positioned at the top of the combustion chamber, with five rows of eleven injectors on each side. The fuel injector diameter is 0.032 mm, while the oxidizer injector diameter is 0.06 mm. The thruster features two propellant inlets on the sides, one for fuel and one for oxidizer, each with a width of 0.6 mm. The fuel and oxidizer enter through the main inlets and are then distributed into ten horizontal channels before being directed to the injectors. The key dimensions of the combustion chambers can be found in Figures 2 and 3.

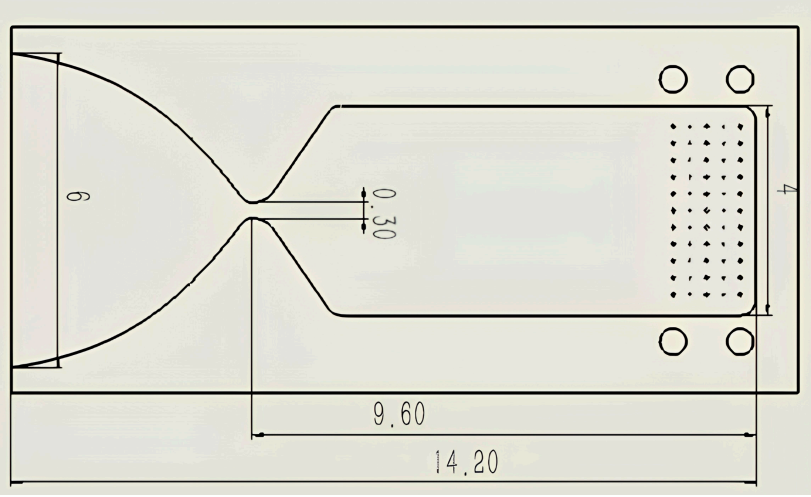

Figure 2. Graphic design drawing of the combustion chamber.

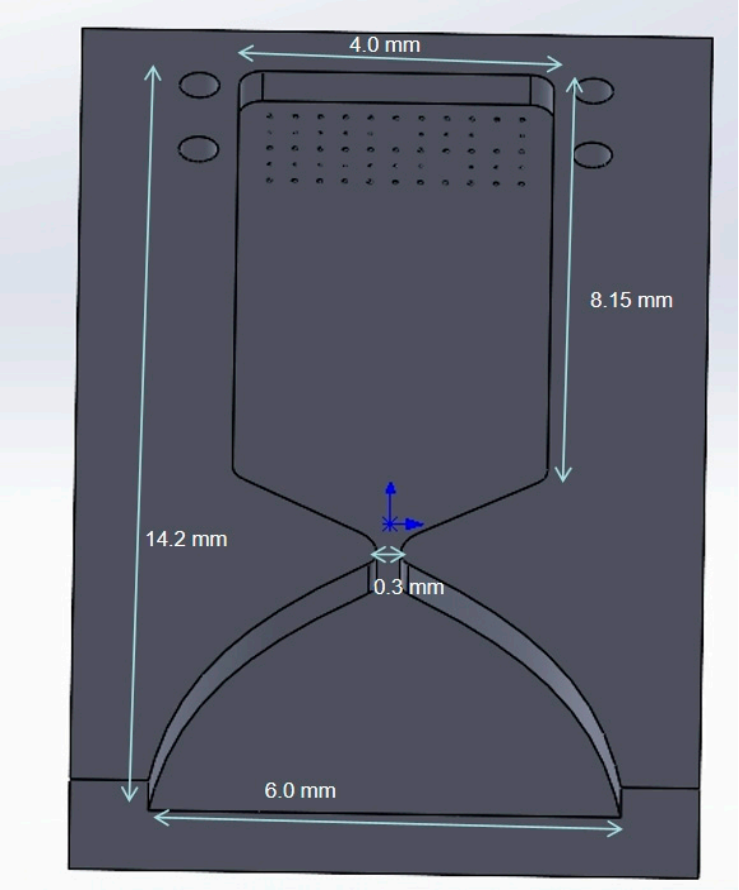

Figure 3. Central section of the baseline design.

The propellant mass flow is about 0.2562 g/s, 0.0513 g/s of fuel, and 0.2049 g/s of oxidizer. The theoretical specific impulse I_{sp} is considered equal to 298.9 s, as mentioned in Section 2.4. The thrust is expected to be 0.75 N, as deduced from the mass flow $\dot{m}$ and specific impulse I_{sp} [23].

$$T = I_{sp}\dot{m}g_0, \quad (2)$$

However, the specific impulse is a theoretical value calculated by software; the actual performance of the thruster might not be so ideal, especially in MEMS. The planar combustion chamber with dimensions inhibits the formation of turbulence. Most of the previous MEMS thrusters operated with a complete or partial laminar flame and lower the specific impulse.

2.4. Methodology

The fluid dynamics of a series of designs are simulated using CFX (Ansys 2023 R2). Figure 4 shows the fluid model. The optimal combustion chamber length is primarily determined by identifying the position at which the concentration of reaction products stabilizes. Another key variable is the expansion ratio—designs with wider exits are tested to evaluate their potential impact on thrust performance. Each design simulation involves approximately 3–3.5 million mesh elements. Due to the small dimension, the Reynolds number of fluids in this thruster is relatively low; the transition between laminar and turbulent flow may occur anywhere within the thruster. Consequently, the turbulence model used is SST, which could well consider the transition of flow. The wall is no-slip. The combustion model employed is Eddy Dissipation. This is a default combustion model in CFX; it uses the rate of dissipation of eddies containing reactants and products to determine the reaction rates [24].

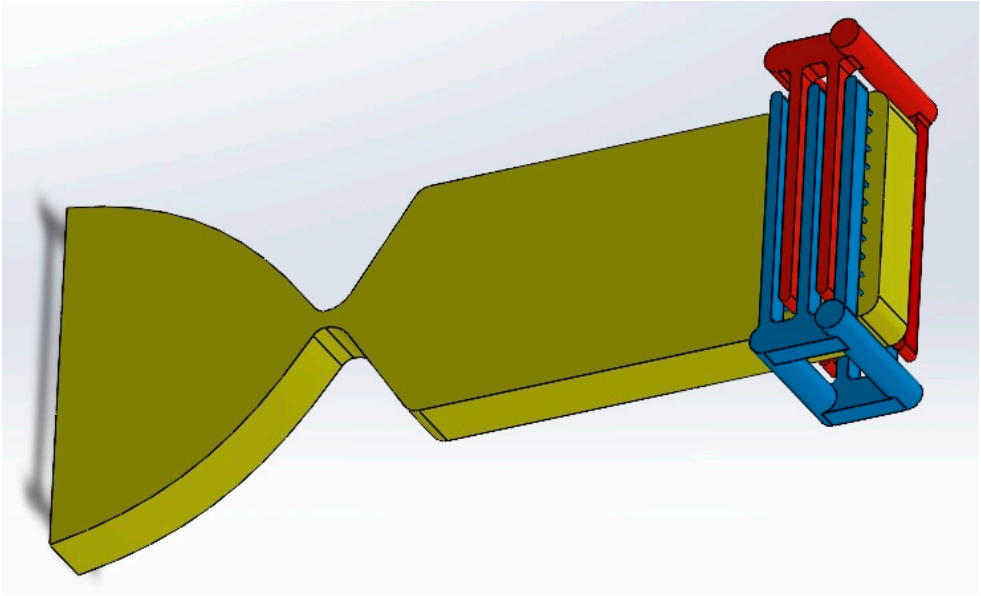

Figure 4. Fluid model of the baseline design, red part represents fuel, blue part represents oxidizer, and yellow part represents mixture.

Due to the characteristics of CFX, the molar coefficients of reactants and products should be determined before simulation. Consequently, the reaction equilibrium in Equation (1) is used in the CFX simulations.

Once the optimal design is identified, the corresponding thruster structure will be developed. A subsequent thermo-mechanical simulation will then be conducted to assess whether the structure can withstand the high temperatures and pressures generated during combustion.

The determination of the expansion ratio is more complex, as it involves balancing performance, volume, and mass. In particular, for a planar nozzle, the expansion ratio increases linearly with the outlet dimension. This results in a significant reduction in the performance gain from a larger outlet, as the increase in specific impulse is counterbalanced by the growth in mass and volume. Excessive mass negatively impacts the thrust-to-weight ratio, while excessive volume limits the number of thrusters that can be produced per unit of wafer, thereby reducing mass production efficiency and increasing overall costs.

Theoretical specific impulse evaluation indicates that when the expansion ratio reaches approximately 20, the subsequent increase in specific impulse slows down, as depicted in Figure 5. Considering that in this type of propulsion system the boundary layer has a strong effect on the fluid behavior and on the performance, worsening as the aspect ratio increases, the preferred value of the aspect ratio should be chosen in the lower range. As a result, the baseline design sets the initial expansion ratio and the upper limit for the final design at 20, since higher expansion ratios may generate a performance reduction, as will be detailed in the following. The expansion ratio, length of the divergent nozzle, and the length of the combustion chamber are interdependent; changes in one will influence the others. Therefore, a compromise must be made between these three factors to accommodate the overall dimensions, especially if the total length of the thruster with an optimal combustion chamber exceeds 15 mm.

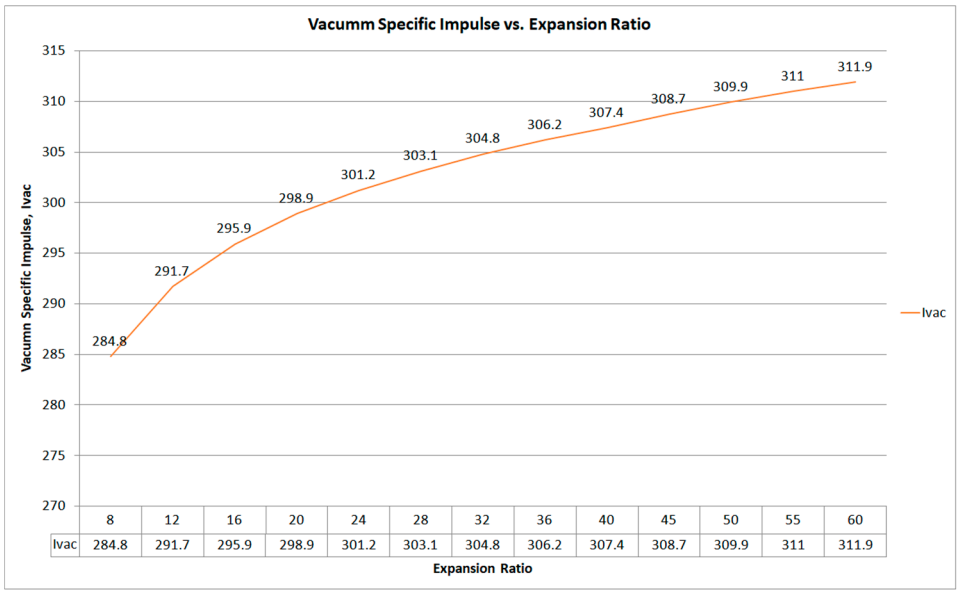

Figure 5. Specific impulse growth with an expansion nozzle calculated by CEARUN. The growth of specific impulse slows down when expansion ratio reaches around 20.

3. Design Optimization

3.1. Description of the Dimensions

Different from a macro-scale rocket, the specific impulse of a micro-thruster will not constantly increase with the expansion ratio. According to research by Dabuek Banuti [24], there is a critical point where the boundary layer begins to expand and take the dominance of the exhaust flow. This is the main reason for the reduction in propulsive performance in micro-scale planar exits as the expansion ratio increases. Compared to a monopropellant thruster with micro-scale planar nozzles developed by DLR, the optimal expansion ratio for this thruster is significantly higher. The optimal expansion ratio of Banuti's planar thruster is around 10; meanwhile, the boundary layer in the baseline design still shows no sign of overgrowth and competing for dominance of the flow. It might be because the bipropellant flow exhibits a higher Reynolds number, which weakens the influence of the boundary layer. Possible contributing factors include the following:

- The dimensions of the nozzle in this research are much larger, and the aspect ratio is lower; it will make the boundary layer gain dominance in the flow more slowly.
- The velocity v of the fluid flow in bipropellant system is much higher than that of monopropellant thruster, with the larger dimension mentioned above. Also, the density ρ and dynamic viscosity μ of the flow are lower due to the temperature and properties of different propellants. The differences might lead to a higher Reynolds number according to the definition of Reynolds number (Equation (3)) [25].

$$\mathrm{Re} = \frac{\rho \upsilon D}{\mu}, \tag{3}$$

To verify this deduction, several models with larger expansion ratios were simulated. The results presented in Figure 6 indicate that this phenomenon occurs when the expansion ratio reaches 40. In these simulations, the chemical reactions were assumed to remain unchanged, as the variation in the products' ratio was sufficiently small to be considered negligible, according to CEARUN. However, since the simulation model has not been specifically validated and refined for the planar configuration, these simulations are not yet accurate or reliable enough to qualitatively analyze the critical position.

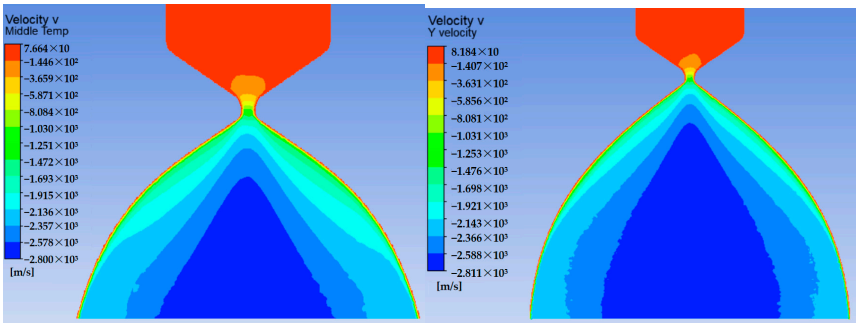

Figure 6. At the exhaust velocity of the additional simulation with expansion ratios of 30 and 40, the acceleration is greatly influenced by the boundary layer. In the second figure, the isovelocity line of the central fluid begins to show a tendency to contract inwards.

3.2. Validation of the Fluid Model

A simulation of the MIT MEMS thruster was conducted to validate the accuracy of the combustion model. The key validation parameter is the specific impulse (I_{sp}). In MIT's research, this parameter is determined through the thrust coefficient (C_F) and the characteristic velocity (C*) [25,26].

$$I_{sp} = C^* C_F \tag{4}$$

The combustion pressures in the MIT thruster experiment were 7 bar, 7.5 bar, and 12.3 bar, with corresponding thrust coefficients (C_F) of 0.95 for both the 7/7.5 bar and 12.3 bar cases. According to Sutton, these values have been corrected to approximate an ideal situation [23]. However, the low expansion ratio and combustion pressures result in nearly a 10% reduction in thrust performance, which is attributed to the split plume observed during the test [26].

The characteristic velocity c^* is calculated based on the temperature, seen in Equation (5) [23].

$$C^* = \sqrt{\frac{RT_0}{M\gamma}} \left(\frac{\gamma+1}{2}\right)^{\frac{\gamma+1}{2(\gamma-1)}} \tag{5}$$

where R is the gas constant, T_0 is the combustion temperature, and M is the average molecular mass of exhaust gas.

The final simulation results for MIT's thruster align well with the adiabatic calculations based on experimental data. The comparison is offered in Table 4. Although the local boiling effect and ambient environment were not considered in the simulation, the agreement between the experimental and calculated results is sufficient to demonstrate the reliability of the simulation model.

Table 4. Comparisons among simulations and calculated and experimental results of MIT MEMS thruster performance.

Result	Combustion Parameter	T_0, K	M, kg/mol	Isp, s
Series 1				
Experiment	P_c = 7 bar, O/F = 2.1	N/A	N/A	145
Calculated				170
Simulated	P_c = 6.7 bar, O/F = 2.1	2574	0.0166	169
Series 2				
Experiment	P_c = 7.5 bar, O/F = 2.4	N/A	N/A	146
Calculated				179
Simulated	P_c = 7.6 bar, O/F = 2.4	3005	0.0182	175

Table 4. *Cont.*

Result	Combustion Parameter	T_0, K	M, kg/mol	Isp, s
Series 3				
Experiment	P_c = 12.3 bar, O/F = 2.4	N/A	N/A	149
Calculated				176
Simulated	P_c = 13.3 bar, O/F = 2.4	3008	0.0182	175

The experimental performance showed a reduction of approximately 15% compared to the calculated and simulated results. The primary causes for this discrepancy were unpredictable losses, which could not be accounted for in theoretical estimations, such as local propellant and coolant boiling, roughness of the combustion chamber inner walls due to MEMS fabrication, and the low ratio between combustion chamber pressure and ambient pressure [26]. For the thruster discussed in this paper, although the exact performance losses will need to be determined through further experiments, it is anticipated that these losses will be smaller due to advances in the manufacturing process and a higher combustion pressure to external pressure ratio.

3.3. Fluid Model and Performance

The simulation results indicate that a combustion chamber length of 5.6 mm is optimal. In the baseline design simulations, the compositional ratios of the combustion products stabilize around this length. The distribution of products can be found in Figure 7, meanwhile the distribution of exhaust velocity can be found in Figures 8–10.

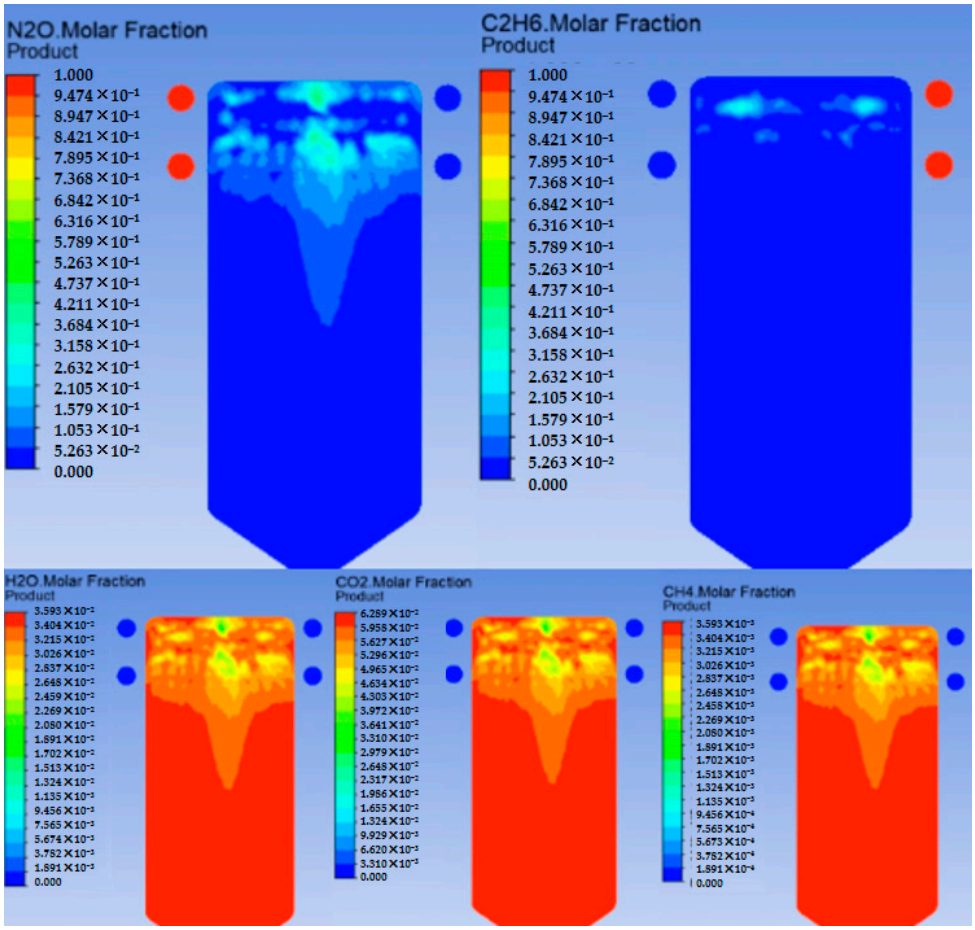

Figure 7. Reactant and product ratios in the baseline design.

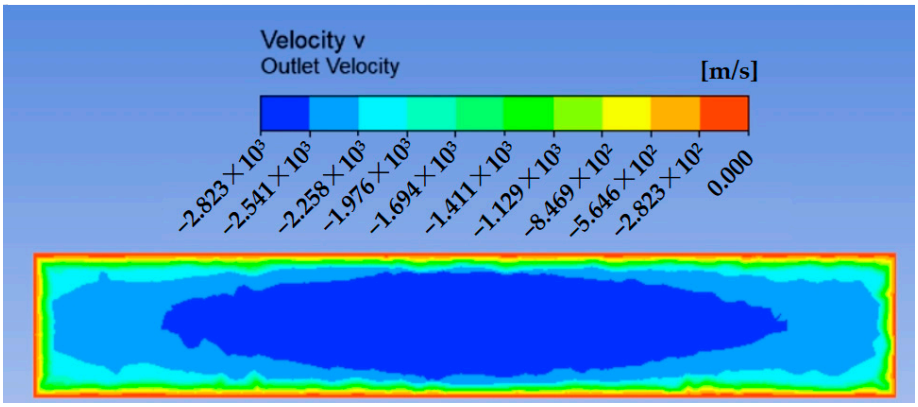

Figure 8. Exhaust velocity (exhaust direction is presented as negative on the scale)

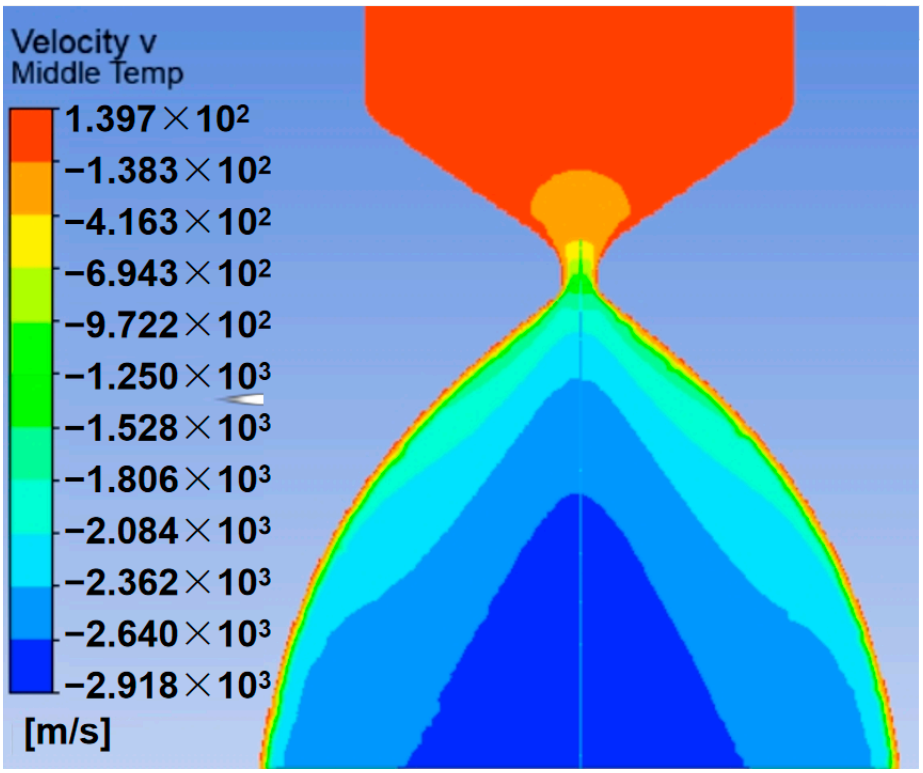

Figure 9. Front view of exhaust velocity in the expansion nozzle (exhaust direction is presented as negative on the scale).

The key dimension and performance of the final fluid model can be found in Table 5:

Table 5. Key parameters of the final design.

Characteristics	Parameters
Chamber height, mm	1
Combustion chamber length, mm	5.6
Total length, mm	10.2
Throat width, mm	0.3
Exit width, mm	6
Expansion ratio	20
Max. combustion temperature, K	3089
Specific impulse, s	243
Estimated thrust, N	0.61
Ave. exhaust velocity, m/s	2623

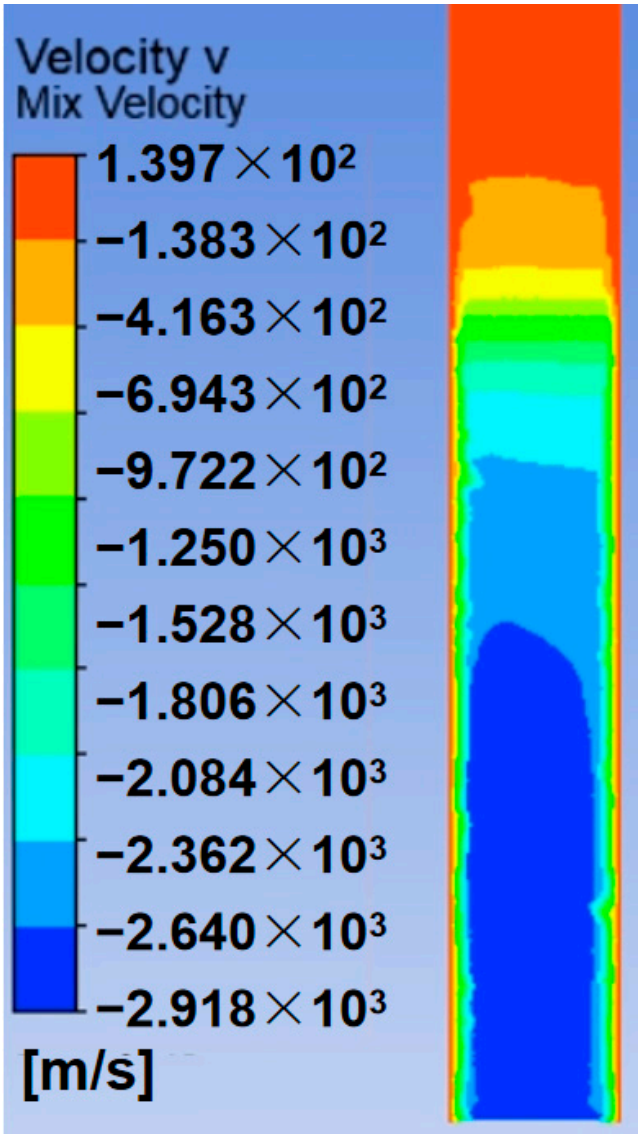

Figure 10. Side view of exhaust velocity in the expansion nozzle (exhaust direction is presented as negative on the scale).

This final design's molar fractions of products are close to the ideal situation, as Table 6 demonstrates. All deviations are lower than 1 percent. The molar fractions of ethane and nitric oxide in the throat are 0.00101 and 0.00150. Considering the 243 s of specified impulse in simulation, this design achieves the expected performance. The flow contour at the exit enlarges significantly. Simulation results show the boundary layer at the nozzle slowly grows and interacts with the central flow. The general flow behavior is similar to the simulation result of viscous flow in a planar nozzle that is performed by DLR [22].

Table 6. Product analysis.

Composition	Setup Fractions	Fraction in CFD	Deviation, ‰
CH_4	0.00360	0.00357	0.83
CO	0.19412	0.19300	0.58
CO_2	0.06278	0.06255	0.37
H_2	0.34728	0.34580	0.43
H_2O	0.03626	0.03574	1.43
N_2	0.35594	0.35680	0.24

4. Final Design

4.1. Thruster Structure and Fabrication Design

The geometry of the thruster is a rectangular body. The dimensions are $11 \times 8 \times 3$ mm^3. The structure is combined by four wafers, which will be bonded together, as Figure 11 shows.

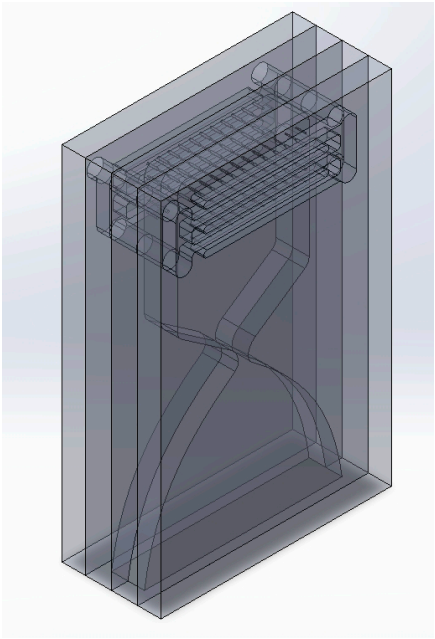

Figure 11. The thruster, measuring $11 \times 8 \times 3$ mm^3 and made from silicon carbide, consists of four bonded layers: Layer 1 contains propellant channels and injectors; Layers 2 and 3 manage propellant distribution and injector alignment; and Layer 4 integrates inlets and inversely aligned channels. This layered design enables compact integration for MEMS-based manufacturing.

The four layers contain the combustion chamber, propellant channels, and nozzle. The thruster also has a slot for embedding ignitors and other electronic components. The patterns on the wafers are fabricated by etching; the process is similar to the milling technique or a subtractive manufacturing version of the fused deposition modeling 3D printing technique. The geometry is etched on a complete wafer and deepened layer by layer. Figure 12 illustrates each of the 4 layers.

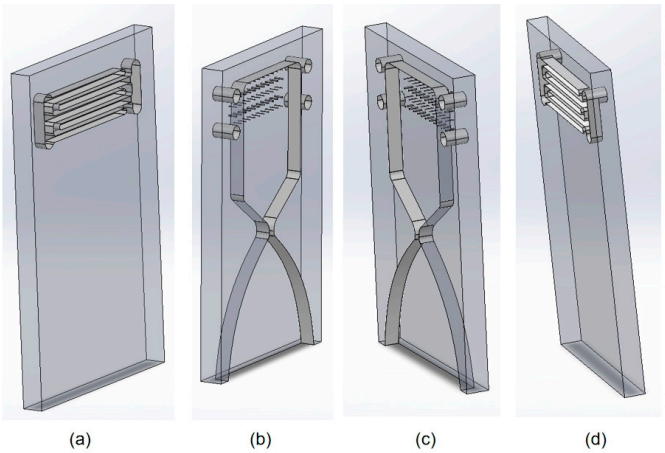

Figure 12. CAD designs of (**a**) Layer 1; (**b**) Layer 2; (**c**) Layer 3; and (**d**) Layer 4.

Layer 1 is one of the side layers. It contains the propellant channels connected to the injectors.

Layer 2 is in the middle, containing half of the injectors and the channels that allow the propellant to flow into Layer 4.

Layer 3 is almost the same as Layer 2. However, the distribution of fuel and oxidizer injectors ensures that each injector will face the other kind of injector. In this case, each fuel stream will collide with an oxidizer stream.

Layer 4 is also similar to Layer 1 but with the inlets. Also, the distribution of fuel and oxidizer channels is inverse with respect to Layer 1.

The thickness of Layer 1 and Layer 2 is 0.7 mm, while that of Layer 3 and Layer 4 is 0.8 mm. Both are standard thicknesses of commercial silicon carbide wafers.

The material is silicon carbide, whose density is 3160 kg/m^3. From the CAD software (Creo Parametric 9.0.0.0), the dry mass of the thruster m = 0.59 g can be deduced. Combining the 0.61 N of thrust, the thrust-to-weight ratio can reach about 105. For a rocket engine, especially a 1N-level thruster, this performance is quite excellent.

Table 7 shows the performance comparison of MEMS thruster with some typical space thrusters. Incorporating a comprehensive propulsion system into consideration can significantly enhance this performance. As previously discussed in Section 2.1, the propellant feed system can be designed as self-pressurized or gas-pressurized, owing to the relatively low combustion pressures involved. This design flexibility allows for a streamlined propulsion supply system with fewer valves and components, thereby reducing complexity and potential points of failure. Consequently, MEMS thrusters equipped with a high-pressure propellant supply system can achieve a lighter and more efficient configuration.

Table 7. Comparison among MEMS thrusters and other ordinary space thrusters for small satellites and low-thrust maneuvers [12,27–30].

Thruster	Specific Impulse, s	Nominal Thrust, N	T/W Ratio
MEMS Thruster	243	0.61	105
MIT Bipropellant	160	1	85
LEROS 1b	317	635	14
Ariane 10N Bi Apogee	220	10	3
Ariane 1N Hydrazine Thruster	230	1	0.35
ECAPS 100 mN HPGP Thruster	200	0.1	2.6

4.2. Thermal Performance

To reduce the simulation difficulty, the surfaces of the thruster are divided into the following three selections: fuel channel (FChannel), oxidizer channel (OChannel), and combustion surface. Figure 13 shows each of the 3 parts.

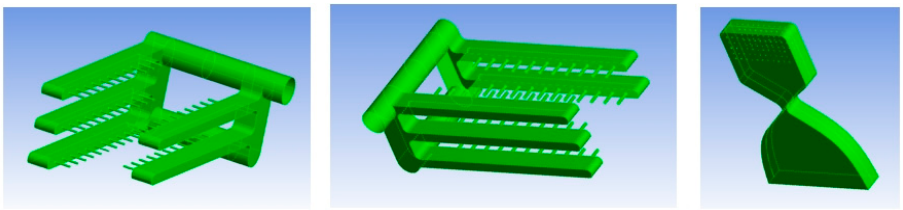

(**a**) (**b**) (**c**)

Figure 13. Regions of the (**a**) fuel channel; (**b**) oxidizer channel; and (**c**) combustion chamber.

The heat transfer coefficient is calculated to provide heat load on the inner wall of the combustion chamber. This calculation is based on the concept of the Nusselt number, Nu, a non-dimensional parameter that describes the heat transfer coefficient. The definition of the Nusselt number is expressed as follows [25]:

$$\mathrm{Nu} = \frac{h_g D}{\kappa} \tag{6}$$

where h_g is the heat convection coefficient, D is the characteristic diameter of the channel, and κ is the heat conduction coefficient. When the temperature is uniform, Nu is 3.66; when the heat flux is uniform, the value is 4.36. In the simulation, the gas in the combustion chamber and the nozzle are regarded as a uniform temperature, and the wall of the propellant channel is regarded as a uniform heat flux. The data can be found in Table 8.

Table 8. h_g in different positions [19,31].

Position	Fuel Channel	Oxidizer Channel	Combustion Chamber
Hydraulic Diameter	0.27 mm	0.27 mm	1.6 mm
Conv. Coefficient	565 W/(m^2·K)	969 W/(m^2·K)	474 W/(m^2·K)
Position	Fuel Channel	Oxidizer Channel	Combustion Chamber
Nusselt Number	4.36	4.36	3.66

When a large rocket is reduced in size, the weight decreases much faster than the thrust, which means that the T:W increases rapidly. Theoretically, the increase in thrust-to-weight ratio is proportional to the decrease in characteristic throat dimensions. However, in practice, the result is not as good as expected because a small propulsion system usually has larger heat losses and less reaction efficiency, which leads to less thrust and specific impulse due to the larger specific surface area and lower characteristic length. In addition, the material of a micro-propulsion system is weaker than that of large rockets, so combustion pressure and temperature cannot reach optimal conditions. However, the proven T:W of earlier designs still easily reached 85, even when the combustion chamber pressure is less than 10% of a common large rocket [12].

The simulation result, listed in Table 9, shows that the highest temperature in the structure is less than 1300 °C. The average value is 1160 °C and the highest temperature on the structure is 1263 °C. This is much lower than the temperature the silicon wafer can withstand. This indicates the fact that the thruster still has a large thermal potential to withstand combustion with higher temperatures and performance. The results of the visualization are also shown in Figure 14.

Table 9. Thermal load setup.

Position	Parameter	Value	Ambient Temperature
Oxidizer Channel	Conv. Coefficient	969 W/(m^2·K)	727 °C
Fuel Channel	Conv. Coefficient	565 W/(m^2·K)	727 °C
Combustion Chamber	Conv. Coefficient	474 W/(m^2·K)	2816 °C
Wall	Emissivity	0.86	0 °C

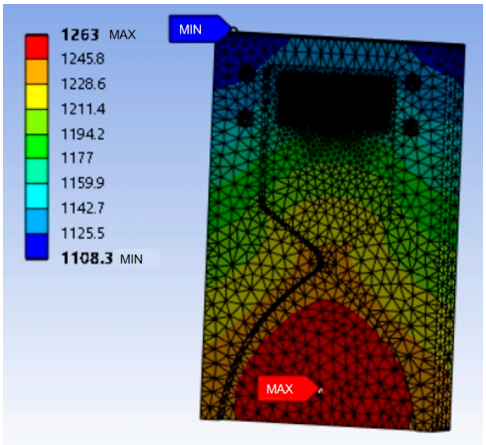

Figure 14. Simulation of temperature distribution, red label is the position of the highest temperature, and blue is that of the lowest temperature.

4.3. Challenge on Experiment

Before proceeding to a detailed experimental design, the following several challenges should be considered:

- Fabrication

Unlike mass-produced products, which benefit from economies of scale through continuous fabrication processes, the low-volume production of MEMS prototypes remains prohibitively expensive, with costs often exceeding €10,000 per unit. While the inherent cost advantages of MEMS fabrication become more pronounced in large-scale production, these benefits diminish in the context of prototype development and iterative testing. This is primarily due to the substantial costs associated with the production of masks and molds, which are required in low-throughput manufacturing scenarios. By the conclusion of this research, there were still no MEMS manufacturers who could provide an economically viable solution for low-scale prototype fabrication. Among the potential solutions, laser processing and micro-machining techniques emerge as promising alternatives, offering the precision and flexibility necessary for efficient prototype development and testing iterations. Also, the machining velocity is faster since there are only 1–3 prototypes to make.

- Ignition

Electrode and heater are both candidates for ignitor. These two options require different etching features on the layers. If the electrode is chosen, another one or more pairs throughout holes will be created, located at the wall of the combustion chamber. These holes will be inserted by tungsten electrodes. The electrodes will create a 1-mm-long arc, which runs through the combustion chamber to ignite the mixture.

For the heater, the tungsten layer will be put in the middle of the combustion chamber. During the operation, the layer will be heated to over 1200 °C to provide the activation energy for combustion. For this option, two small slots are etched above the combustion chamber to embed the wire of the heater. They protrude from the top of the thruster and connect to the power source.

No matter which method is chosen, a new challenging fabrication process will be added. Most are about sealing after new features are created. In addition, for the heater option, the heater needs to be embedded before the bonding process. All those additional techniques will lead to more technical challenges and costs, which are unworthy and unnecessary for prototype fabrication and low-volume manufacture.

Consequently, all features for the ignition system will not be designed in this phase. The two ignitors will be manufactured independently. In the experiment, ignitors will be inserted into the combustion chamber through the outlet. Other objectives of this experiment include the collection of ignition performance (time, power requirement, reliability, lifetime, etc.) and the choice of a better option for the next step of development.

It should be noted that inserting two electrodes from the outlet is impossible since the smallest cross-section area is only 0.3 mm^2 (cross-section area of the throat). Consequently, like what Adam London did in his Ph.D. thesis [26] the arc creator will be produced by a pair of twisted magnets.

5. Conclusions

The simulation phase of this design has been completed. Overall, the combustion characteristics, including product fractions and thrust performance, closely align with the expectations, which provides preliminary evidence of the simulation's reliability. Based on these results, further prototyping and refinement can proceed.

The simulation results demonstrate that the geometry and structure of the system exhibit promising performance, suggesting significant potential for further development.

Compared to electric propulsion, chemical propulsion offers a substantially higher thrust for the same mass and volume. Additionally, the bipropellant design enhances the specific impulse of the MEMS thruster when compared to traditional monopropellant systems. The compact geometry and efficient structure of MEMSs enable the integration of all necessary functions with a reduced mass and volume. In summary, the bipropellant MEMS propulsion system provides an optimal balance between specific impulse, thrust, structural simplicity, and mass, enabling small spacecraft to perform a broader range of orbital maneuvers, including impulsive orbit transfer. This advancement opens new possibilities for small satellite missions.

The forthcoming stages of this research will primarily focus on optimizing ignition techniques and further refining the associated fabrication methods. An alternative small-scale production method is necessary for experiment and iteration.

Author Contributions: Conceptualization, Y.Z. and F.B.; methodology, Y.Z.; software, Y.Z.; investigation, Y.Z. and S.L.; resources, F.P., F.B., X.Z. and G.X.; data curation, Y.Z.; writing—original draft preparation, Y.Z.; writing—review and editing, F.P., S.L., G.X., X.Z. and T.W.; visualization, Y.Z. and T.W.; supervision, X.Z.; funding acquisition, F.P. All authors have read and agreed to the published version of the manuscript.

Funding: This research received no external funding.

Data Availability Statement: The raw data supporting the conclusions of this article will be made available by the authors upon reasonable request.

Conflicts of Interest: The authors declare no conflicts of interest.

Abbreviations

The following abbreviations are used in this manuscript:

MEMS	Micro–Electro-Mechanical System
O/F ratio	oxidizer-to-fuel ratio
DLR	German Aerospace Center
T:W ratio	thrust-to-weight ratio

References

1. Fortescue, P.; Swinerd, G.; Stark, J. *Spacecraft Systems Engineering*; John Wiley & Sons: Hoboken, NJ, USA, 2011; ISBN 111997836X.
2. Bouwmeester, J.; Guo, J. Survey of Worldwide Pico-and Nanosatellite Missions, Distributions and Subsystem Technology. *Acta Astronaut.* **2010**, *67*, 854–862. [CrossRef]
3. Oh, H.-U.; Kim, T.-G.; Han, S.-H.; Lee, J. Verification of MEMS Fabrication Process for the Application of MEMS Solid Propellant Thruster Arrays in Space through Launch and On-Orbit Environment Tests. *Acta Astronaut.* **2017**, *131*, 28–35. [CrossRef]
4. Xu, J.; Zhang, J.; Li, F.; Liu, S.; Ye, Y.; Shen, R. A Review on Solid Propellant Micro-Thruster Array Based on MEMS Technology. *FirePhysChem* **2024**, *4*, 95–106. [CrossRef]
5. Alnaqbi, S.; Darfilal, D.; Swei, S.S.M. Propulsion Technologies for CubeSats. *Aerospace* **2024**, *11*, 502. [CrossRef]
6. Pallichadath, V.; Turmaine, L.; Melaika, A.; Gelmi, S.; Ramisa, M.V.; Rijlaarsdam, D.; Silva, M.A.C.; Guerrieri, D.C.; Uludag, M.S.; Zandbergen, B.; et al. In-Orbit Micro-Propulsion Demonstrator for PICO-Satellite Applications. *Acta Astronaut.* **2019**, *165*, 414–423. [CrossRef]
7. Liu, B.; Li, X.; Yang, J.; Gao, G. Recent Advances in MEMS-Based Microthrusters. *Micromachines* **2019**, *10*, 818. [CrossRef] [PubMed]
8. Kvell, U.; Puusepp, M.; Kaminski, F.; Past, J.-E.; Palmer, K.; Grönland, T.-A.; Noorma, M. Nanosatellite Orbit Control Using MEMS Cold Gas Thrusters. *Proc. Est. Acad. Sci.* **2014**, *63*, 279. [CrossRef]
9. Fontanarosa, D.; Francioso, L.; De Giorgi, M.G.; Vetrano, M.R. MEMS Vaporazing Liquid Microthruster: A Comprehensive Review. *Appl. Sci.* **2021**, *11*, 8954. [CrossRef]
10. Cervone, A.; Zandbergen, B.; Guerrieri, D.C.; De Athayde Costa e Silva, M.; Krusharev, I.; van Zeijl, H. Green Micro-Resistojet Research at Delft University of Technology: New Options for Cubesat Propulsion. *CEAS Space J.* **2017**, *9*, 111–125. [CrossRef]
11. Seran Hall Thruster. Available online: https://seransystems.com/?page_id=55 (accessed on 4 December 2024).

12. London, A.P.; Epstein, A.H.; Kerrebrock, J.L. High-Pressure Bipropellant Microrocket Engine. *J. Propuls. Power* **2001**, *17*, 780–787. [CrossRef]
13. Dwivedi, S.K.; Vishwakarma, M. Hydrogen Embrittlement in Different Materials: A Review. *Int. J. Hydrogen Energy* **2018**, *43*, 21603–21616. [CrossRef]
14. Guerrieri, D.C.; Silva, M.A.C.; Cervone, A.; Gill, E. Selection and Characterization of Green Propellants for Micro-Resistojets. *J. Heat Transfer* **2017**, *139*, 102001. [CrossRef]
15. Janzer, C.; Richter, S.; Naumann, C.; Methling, T. "Green Propellants" as a Hydrazine Substitute: Experimental Investigations of Ethane/Ethene-Nitrous Oxide Mixtures and Validation of Detailed Reaction Mechanism. *CEAS Space J.* **2022**, *14*, 151–159. [CrossRef]
16. Hebden, R.; Bielby, R.; Baker, A.; Mistry, S.; Köhler, J.; Stenmark, L.; Sanders, B.; Moerel, J.-L.; Halswijk, W.; Rops, C.; et al. The Development and Test of a Hydrogen Peroxide Monopropellant Microrocket Engine Using MEMS Technology. In Proceedings of the ESTEC 2005, Noordwijk, The Netherlands, 3–5 October 2005.
17. Jiang, L.; Cheung, R. A Review of Silicon Carbide Development in MEMS Applications. *Int. J. Comput. Mater. Sci. Surf. Eng.* **2009**, *2*, 227. [CrossRef]
18. Ivashchenko, V.I.; Turchi, P.E.A.; Shevchenko, V.I. Simulations of the Mechanical Properties of Crystalline, Nanocrystalline, and Amorphous SiC and Si. *Phys. Rev. B—Condens. Matter Mater. Phys.* **2007**, *75*, 85209. [CrossRef]
19. Munro, R.G. Material Properties of a Sintered α-SiC. *J. Phys. Chem. Ref. Data* **1997**, *26*, 1195–1203. [CrossRef]
20. Liu, J.T.; Ma, Y.F.; Gao, Y. A Review of the Vaporizing Liquid Microthruster Technology. In Proceedings of the 2014 ISFMFE-6th International Symposium on Fluid Machinery and Fluid Engineering; Institution of Engineering and Technology, Wuhan, China, 22–25 October 2014; p. 096(1-3).
21. Micro-Electromechanical Systems. Available online: https://encyclopedia.pub/entry/42347 (accessed on 24 June 2024).
22. Banuti, D.T.; Grabe, M.; Hannemann, K. Flow Characteristics of Monopropellant Micro-Scale Planar Nozzles. *Aerosp. Sci. Technol.* **2019**, *86*, 341–350. [CrossRef]
23. Sutton, G.P.; Biblarz, O. *Rocket Propulsion Elements*; John Wiley & Sons: Hoboken, NJ, USA, 2011; ISBN 1118174208.
24. Ertesvåg, I.S.; Magnussen, B.F. The Eddy Dissipation Turbulence Energy Cascade Model. *Combust. Sci. Technol.* **2000**, *159*, 213–235.
25. Buresti, G. *Elements of Fluid Dynamics*; World Scientific Publishing Company: Singapore, 2012; Volume 3, ISBN 1908977043.
26. London, A.P. Development and Test of a Microfabricated Bipropellant Rocket Engine. Ph.D. Dissertation, Massachusetts Institute of Technology, Cambridge, MA, USA, 2000.
27. LEROS 1b Apogee Engine. Available online: https://www.nammo.com/wp-content/uploads/2021/03/2021-Nammo-Westcott-Liquid-Engine-LEROS1B.pdf (accessed on 28 June 2024).
28. 20N BI-PROPELLANT THRUSTER. Available online: https://www.space-propulsion.com/spacecraft-propulsion/hydrazine-thrusters/20n-hydrazine-thruster.html (accessed on 28 June 2024).
29. Regulus Electric Propulsion. Available online: https://www.space-propulsion.com/brochures/hydrazine-thrusters/hydrazine-thrusters.pdf (accessed on 28 June 2024).
30. ECAPS 100 MN HPGP Thruster. Available online: https://satsearch.co/products/ecaps-100-m-n-hpgp-thruster (accessed on 15 February 2025).
31. Liu, L.; Yang, L.; Ma, H.; Luo, J.; Xiao, X.; Zhao, C.; Zhang, J.; Wang, G.; Wang, Y. Oxidation Induced Emissivity Evolution of Silicon Carbide Based Thermal Protection Materials in Hypersonic Environments. *J. Asian Ceram. Soc.* **2021**, *9*, 1506–1515. [CrossRef]